International Journal of Thermofluids 33 (2026) 101616

Contents lists available at ScienceDirect

International Journal of Thermofluids

journal homepage: www.sciencedirect.com/journal/international-journal-of-thermofluids

# Coupled electromagnetic–thermal modeling of ferromagnetic implants in porous tissue for hyperthermia

Pongsavat Savatdipap [a], Teerapot Wessapan [a,*], Manop Yamfang [a], Phadungsak Rattanadecho [b]

[a] Department of Mechanical Engineering, Faculty of Engineering, Rajamangala University of Technology Thanyaburi, Pathumthani 12110, Thailand
[b] Center of Excellence in Electromagnetic Energy Utilization in Engineering (CEEE), Department of Mechanical Engineering, Faculty of Engineering, Thammasat University (Rangsit Campus), Pathumthani 12120, Thailand

ARTICLE INFO

*Keywords:*
Ferromagnetic implant hyperthermia
Porous tissue
Heat transfer
Flow dynamics
Hyperthermia treatment planning

ABSTRACT

Ferromagnetic implant hyperthermia (FIH) involves heat generation from metallic implants via eddy-current and magnetic hysteresis losses. Conventional Pennes-based models neglect convective transport in porous tissue, limiting accuracy near implants. This work develops an experimentally validated electromagnetic–thermal framework that incorporates both Pennes and porous-media formulations to examine implant-mediated heating. The porous-media model shows improved agreement with liver-phantom experiments, particularly in the transient regime, due to explicit treatment of interstitial convection. A key finding is that heating increases with magnetic flux density and implant diameter but exhibits a peak at a critical implant size, beyond which thermal dissipation dominates and restricts further temperature rise. This nonlinear transition arises from the competition between eddy-current power deposition and conduction–convection heat losses in surrounding tissue. Tissue porosity further modulates these trends by enhancing convective spreading of thermal energy. These results identify field strength, implant geometry, and tissue microstructure as governing parameters for controlled and predictable implant-based hyperthermia. The validated framework provides a physically grounded basis for optimizing implant design and magnetic-field excitation in pre-clinical FIH treatment planning and device design.

## 1. Introduction

Magnetic-field-based hyperthermia has undergone continuous development over recent decades [1–4], but many studies have emphasized clinical demonstrations rather than addressing limitations in precise temperature control and penetration depth. The major challenge is to achieve accurate temperature control to prevent thermal injury to adjacent healthy tissues throughout the procedure and to ensure that the applied magnetic field attains sufficient strength at deeper locations.

In conventional systems, heating coils are generally constructed from copper wire or copper tubing [5] and positioned above the target region to generate an alternating magnetic field [6–8]. The induced eddy currents generate Joule heating in metallic needles, leading to localized tumor cell destruction. However, because the magnetic-field intensity decays rapidly with distance, induction heating is typically effective only for relatively shallow regions [9–11]. For deeper targets, inadequate heating due to field attenuation has motivated coil optimization and multi-coil configurations [12–14]. Flexible coil designs have also been introduced to reduce inductance and increase magnetic-field penetration, offering improvements over conventional copper coils [15–17].

This motivates a closer examination of how implant–tissue interactions, particularly the role of porous tissue, govern heat dissipation and local temperature rise. Compared with nanoparticle-based magnetic hyperthermia, the proposed induction-activated implant generates heat directly within a conductive ferromagnetic implant through eddy-current Joule heating and magnetic losses. This mechanism enables localized heating that can be tuned through implant geometry and coil excitation parameters without requiring nanoparticle injection. However, several practical considerations remain, including the need for implant placement and eventual device clearance, sensitivity to

* Corresponding author.
*E-mail addresses:* pongsavat_s@mail.rmutt.ac.th (P. Savatdipap), teerapot_w@rmutt.ac.th (T. Wessapan), manop_y@rmutt.ac.th (M. Yamfang), ratphadu@engr.tu.ac.th (P. Rattanadecho).

https://doi.org/10.1016/j.ijft.2026.101616

Available online 6 April 2026

coil–implant alignment, and the possibility of localized thermal hotspots near the metal–tissue interface. Despite these limitations, implant-mediated induction heating provides a controllable mechanism for localized energy deposition from a heat-transfer perspective. Selected recent studies on electromagnetic dissipation and magnetic-loss materials are briefly cited to contextualize loss mechanisms that are relevant to induction-based heating [31,32].

Natural or interstitial convection can significantly influence thermal behavior during localized hyperthermia. For example, Ooi et al. [29] reported that buoyancy-induced flow within biological tissue modifies the temperature distribution in gold-nanorod-assisted photothermal therapy, underscoring the importance of including convective effects in thermal modeling of biological media. Moreover, conventional bioheat models often assume instantaneous thermal diffusion, which may limit their accuracy in transient heating problems. Gupta and Srivastava [30] demonstrated this via a time-dependent thermal evaluation employing a non-Fourier theoretical framework to characterize the temperature response of tissue-mimicking materials subjected to high-intensity focused ultrasound (HIFU) exposure, while Andreozzi et al. [33] provided a broader overview of mathematical models and modulated-heating protocols for thermal ablation, emphasizing the importance of selecting a thermal model that is consistent with the spatial and temporal scales of the treatment problem. Fig. 1 schematically illustrates the FIH configuration and implant–tissue–coil arrangement considered in this study.

In this context, the present study focuses on porous tissue as a key factor influencing convective heat dissipation and reshaping the temperature distribution around the implant. The resulting flow-driven heat-transfer patterns in the porous-media formulation differ substantially from those predicted by the conventional Pennes bioheat model [18,19]. Porous-media formulations have long been advocated to capture interstitial-flow–driven convection and effective thermal properties beyond Pennes' perfusion source term [21–23]. Recent numerical analyses of convection in porous domains with internal volumetric sources further reinforce the need for explicit flow–heat coupling near heated inclusions [20]. Related studies by the authors demonstrated that flow effects significantly influence thermal distribution in ablation [24] and that transient thermal evolutions are modulated by tissue–vessel interactions [25], motivating the fully coupled EM–thermal porous-media framework adopted here.

Implant features such as material, geometry, size, and insertion depth are key factors governing local tissue heating under high-intensity near-field electromagnetic exposure. These characteristics influence not only the magnitude of heating but also the spatial distribution of temperature rise in surrounding tissue. Accordingly, detailed modeling is required to capture the coupled electromagnetic and thermal responses associated with different implant configurations.

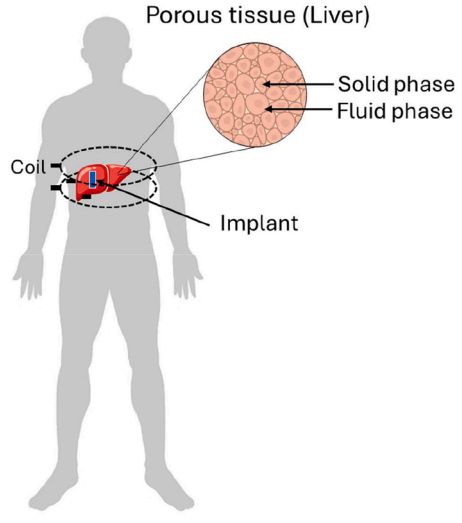


**Fig. 1.** Schematic illustration of ferromagnetic implant hyperthermia (FIH) showing the placement of a ferromagnetic implant within porous liver tissue.

The thermal response of tissue surrounding metallic implants is investigated through a coupled electromagnetic–thermal modeling framework that considers implant material, geometry, size, and depth. Electromagnetic fields are described using frequency-domain Maxwell's equations, which are coupled with tissue heat transfer predicted by the Pennes bioheat and porous-media formulations. The physical model represents layers of tissue and metallic implants exposed to an alternating electromagnetic field generated by an induction coil. Model predictions were validated against experimental temperature measurements in tissue phantoms, confirming good agreement and reduced error relative to conventional approaches. The results reveal the existence of a thermally and therapeutically relevant critical-size threshold and provide physics-based design guidelines for achieving controlled, predictable, and safe implant-mediated heating.

## 2. Formulation of the problem

Ferromagnetic Implant Hyperthermia (FIH) is a promising approach for localized tumor treatment, where metallic implants embedded in tissue are heated under alternating electromagnetic fields. However, the prediction of temperature distribution in implant-embedded tissue remains challenging because conventional bioheat models neglect convective transport due to tissue porosity, potentially leading to inaccuracies in treatment planning. Tissue porosity, which represents microscopic voids filled with blood or interstitial fluid, plays a significant role in modulating heat dissipation. Despite its importance, the influence of porous structures on implant-induced heating has not been thoroughly examined.

To address this gap, the present study integrates controlled ex vivo phantom experiments with numerical simulations. Fresh bovine liver was used as a biological tissue mimic, and temperature evolution near an embedded metallic implant was measured using fiber-optic sensors. These measurements provided high-resolution reference data for validating the computational framework.

The computational framework was developed using a two-dimensional axisymmetric representation to model electromagnetic power deposition and heat transfer in implant-embedded tissue, with thermophysical properties summarized in Table 1. The axisymmetric configuration (Fig. 2) captures the essential physics of implant–tissue interactions while enabling efficient simulation of the parameter space examined in this study. Although implant geometry is known to influence electromagnetic coupling, the quantitative relationship between implant diameter and the resulting thermal response has not been systematically investigated. Prior studies generally assume that heating increases monotonically with implant size; however, the interplay between Joule heating and tissue-dependent thermal dissipation suggests the possibility of a nonlinear response. This motivates the present investigation into whether a critical implant size exists beyond which further increases in diameter fail to enhance, and may even limit, temperature rise—a phenomenon not previously characterized in ferromagnetic implant hyperthermia.

## 3. Numerical model and methods

To investigate the coupled electromagnetic and thermal responses of implant–tissue systems, a computational scheme utilizing a finite-element-based approach was adopted for the analysis. The computational setup simultaneously resolves electromagnetic wave interactions and the evolving thermal response of the implant and surrounding porous biological tissues. Both the conventional Pennes bioheat model and the porous-media (Brinkman) formulation were implemented to assess the influence of tissue porosity on heat dissipation and

**Table 1**
Materials properties [27,28].

| Material | Density ($\rho$) (kg/m$^3$) | Thermal conductivity ($k$) (W/m.K) | Heat capacity ($C$) J/(kg·K) | Blood perfusion rate ($\omega_b$) (1/s) | Electrical conductivity ($\sigma$) (S/m) | Relative permittivity ($\varepsilon_r$) | Relative permeability ($\mu_r$) |
|---|---|---|---|---|---|---|---|
| Liver (bovine) | 1060 | 0.56 | 3639 | 0.0036 | 1.69 | 43.04 | 1 |
| Air | 1.29 | 0.025 | 1004 | - | 0 | 1 | 1 |
| Stainless Steel 410 | 7880 | 25 | 460 | - | 1.74e6 | 1 | 700 |

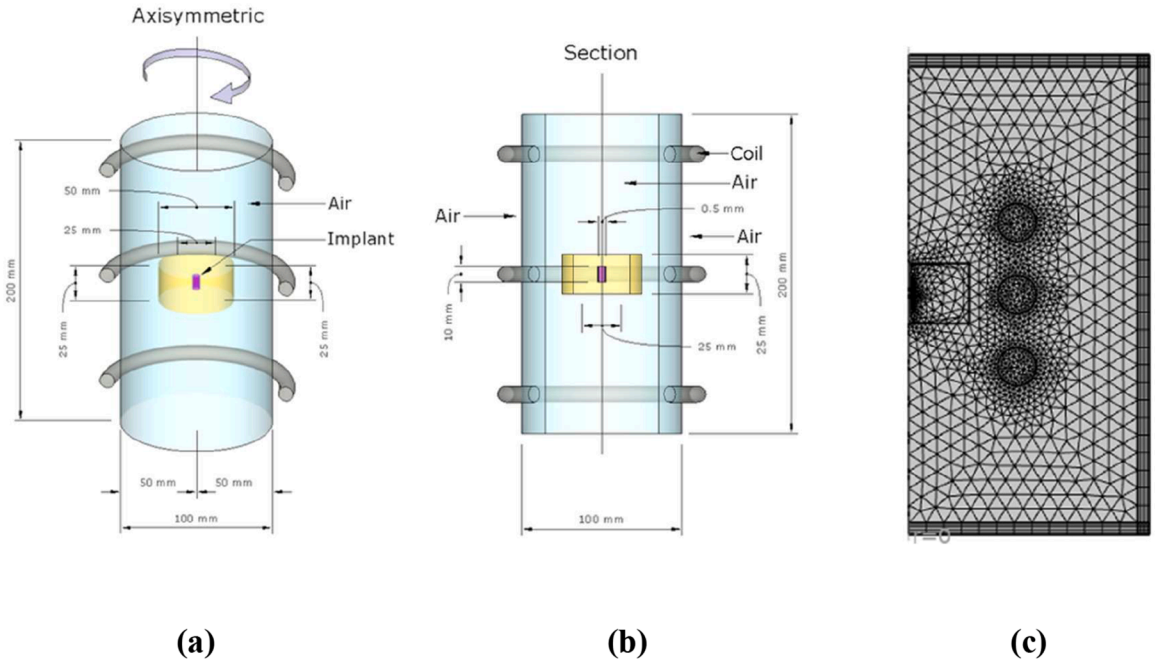


**Fig. 2.** Schematic of the numerical model used in this study: (a) Schematic 3D view of the axisymmetric configuration, (b) Section view showing the implant, coil, and tissue domains, and (c) mesh distribution.

temperature distribution. The simulations were carried out under conditions consistent with the phantom experiments described in Section 2, enabling direct comparison between numerical predictions and measured data.

In the present work, the heating process occurs over time scales of several seconds and spatial scales of millimeters, for which classical Fourier-based heat transfer combined with porous convection is generally sufficient to describe the dominant thermal transport mechanisms. In view of the broader thermal-ablation modeling landscape summarized by Andreozzi et al. [33], the LTE porous-media formulation adopted here represents a balanced approach that improves upon the Pennes model by incorporating convective transport while avoiding the introduction of poorly characterized parameters required by more complex formulations. The following subsections outline the physical model configuration, the governing mathematical formulations, the prescribed spatial–thermal constraints, as well as the computational procedures adopted in this study.

### 3.1. Physical model

In this study, a two-dimensional (2D) axisymmetric representation was employed to capture the vertical cross-section of a three-dimensional implant–tissue configuration. The tissue phantom was modeled as a homogeneous cylindrical domain (25 mm in diameter and 25 mm in height) prepared from bovine liver, as described in Section 2. A stainless-steel rod with a diameter of 0.5 mm and a length of 10 mm was embedded centrally to replicate a ferromagnetic implant. The thermal and electrical properties of the materials used in the simulations are summarized in Table 1 [27,28].

Both tissue and implant were assumed to be electrically and thermally isotropic, with constant properties throughout the heating process. Phase change, chemical reactions, and thermo-mechanical effects were neglected, consistent with prior EM-heating studies [25]. The induction coil was represented as a three-turn circular loop (10-mm diameter) positioned coaxially with the implant to generate the alternating magnetic field; coil geometry was included in the model, whereas operating conditions (frequency, input power) are specified in Section 4.

Fig. 2 illustrates the numerical model used in this study, including the tissue domain, implant geometry, coil representation, and mesh distribution. Fig. 3 shows the corresponding experimental setup used for model validation, including the liver phantom, embedded implant, induction coil arrangement, and fiber-optic temperature sensors. The experimental configuration in Fig. 3 provides the reference conditions against which numerical predictions were compared.

### 3.2. Equations for electromagnetic field analysis

The electromagnetic heating mechanism considered in this study is governed by induction effects generated by an alternating magnetic field interacting with a conductive metallic implant. In such situations, the induced electric currents and associated Joule heating originate from time-varying magnetic flux according to Faraday's law. Consequently, a full electromagnetic formulation based on Maxwell's equations is required to accurately describe the coupling between electric fields,

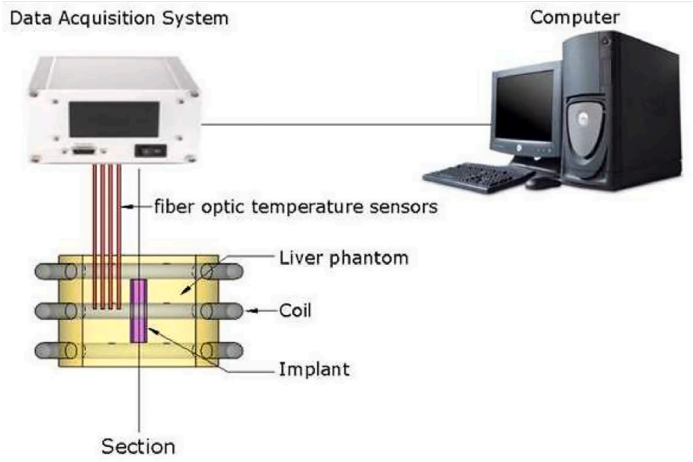


(a)

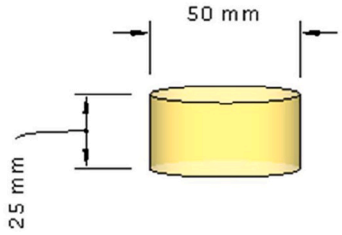


(b)

**Fig. 3.** Experimental setup for ferromagnetic implant hyperthermia: (a) Schematic illustration of the experimental configuration showing the induction coil, embedded implant, and fiber-optic temperature sensors connected to the data acquisition system, and (b) liver phantom geometry used for temperature measurement.

magnetic fields, and induced current densities.

Simplified formulations such as Laplace equations are generally applicable to electrostatic or magnetostatic conditions where time-dependent induction effects are negligible. However, these formulations cannot capture the generation of eddy currents responsible for heating in induction-based hyperthermia systems. Similarly, classical electromagnetic wave equations are primarily used to describe wave propagation in free space or dielectric media and are less suitable for induction-dominated regimes where electromagnetic diffusion in conductive materials is the dominant mechanism. Because the operating frequencies considered in this study correspond to a quasi-static electromagnetic regime, the problem is more appropriately represented using the frequency-domain Maxwell formulation expressed through the magnetic vector potential. This approach allows accurate evaluation of induced current density and volumetric electromagnetic power dissipation, which subsequently acts as the heat source in the coupled thermal analysis.

To model the electromagnetic field (EMF) acting on the implant–tissue system, a two-dimensional (2D) axisymmetric geometry was adopted. The tissue and implant were treated as electrically isotropic with constant dielectric properties over the simulated temperature range. The interaction with open space was represented by truncating the exterior with infinite-element domains, and a magnetic-insulation boundary was imposed at the outer boundary to suppress reflections. Within this setting, a frequency-domain (time-harmonic) formulation was employed.

Following the simplified representation used in prior work, the electromagnetic field propagation is expressed via Maxwell's relations as:

$$\nabla \times \mathbf{H} = \mathbf{J}, \tag{1}$$

$$\mathbf{B} = \nabla \times \mathbf{A}, \tag{2}$$

$$\boldsymbol{E} = -j\omega\mathbf{A}, \tag{3}$$

$$\mathbf{J} = \sigma\mathbf{E} + j\omega\mathbf{D}, \tag{4}$$

where **A** is the magnetic vector potential (Wb/m), **D** is the electric displacement or electric flux density (C/m$^2$), **J** is the current density (A/m$^2$), **H** is the magnetic field intensity (A/m), **B** is the magnetic flux density (T), **E** is the electric field intensity (V/m), $\sigma$ denotes the electrical conductivity of the medium (S/m), $j = \sqrt{(-1)}$, and $\omega = 2\pi f$ is the angular frequency of the magnetic field (rad/s).

The constitutive relations are

$$\mathbf{D} = e_0 e_r \mathbf{E}, \tag{5}$$

$$\mathbf{B} = \mu_0 \mu_r \mathbf{H}, \tag{6}$$

where $\varepsilon_r$ and $\mu_r$ are the relative permittivity and permeability of the medium. $\varepsilon_0 = 8.8542 \times 10^{-12}$ F/m is the permittivity of free space and $\mu_0 = 1.257 \times 10^{-6}$H/m is the permeability of free space.

### 3.3. Equations for heat transfer in the implants

Heat transfer within the metallic implant is modeled as transient conduction in a homogeneous, isotropic solid on the 2D axisymmetric domain. Over the simulated temperature range, thermophysical properties are taken as constant; phase change and chemical reactions are neglected; perfect thermal contact at the implant–tissue interface is assumed (continuity of temperature and normal heat flux); and thermomechanical effects are not considered.

The temperature field in the implant satisfies

$$\rho C\frac{\partial T}{\partial t} = \nabla\cdot(k\nabla T) + Q_e, \tag{7}$$

where $\rho$(kg/m$^3$), $C$ (J/(kg·K), and $k$ (W/m. K) are the density, specific heat, and thermal conductivity of the implant, respectively.

The electromagnetic volumetric heat source is decomposed as

$$Q_e = Q_{rh} + Q_{ml}, \tag{8}$$

with the resistive (ohmic) loss and magnetic loss given by

$$Q_{rh} = \frac{1}{2}\mathrm{Re}(\mathbf{J}\cdot\mathbf{E}^*), \tag{9}$$

$$Q_{ml} = \frac{1}{2}\mathrm{Re}(i\omega\mathbf{B}\cdot\mathbf{H}^*). \tag{10}$$

Here **E, H, B**, and **J** are the phasor (complex-amplitude) fields obtained from the EM formulation in Section 3.2; $i=\sqrt{(-1)}$, and $\omega = 2\pi f$; $Re(\cdot)$ denotes the real part; and $(\cdot)^*$ is the complex conjugate, yielding the correct time-averaged power density in a harmonic regime. For non-ferromagnetic metals $Q_{ml}$=0.

In ferromagnetic implant hyperthermia, the volumetric electromagnetic heat source in the implant is decomposed into resistive (eddy-current) loss $Q_{rh}$ and magnetic loss $Q_{ml}$ (Eqs. (9) and 10). To quantify the relative importance of these mechanisms, we evaluate the integrated power contributions inside the implant volume $V_i$:

$$P_{rh} = \int_{V_i} Q_{rh}\,dV, \quad P_{ml} = \int_{V_i} Q_{ml}\,dV, \quad P_{tot} = P_{rh} + P_{ml}. \tag{11}$$

The ratios $P_{rh}/P_{tot}$ and $P_{ml}/P_{tot}$ provide a direct measure of whether the heating is dominated by eddy currents or by magnetic losses under the present frequency and field conditions. This comparison is also useful for assessing model simplifications: if $P_{ml} \ll P_{rh}$, the predictive model may be simplified by neglecting magnetic losses; conversely, if $P_{ml}$ is non-negligible, both terms should be retained. We note that $Q_{ml}$ requires a magnetic-loss characterization (e.g., complex permeability or an equivalent hysteresis-loss representation) of the implant material; therefore, uncertainties in loss data should be reported and may motivate a sensitivity analysis.

Continuity at the implant–tissue interface enforces

$$T_i = T_t, \qquad -k_i\nabla T\cdot\mathbf{n} = -k_t\nabla T\cdot\mathbf{n}, \tag{12}$$

with subscripts $i$ and $t$ denoting implant and tissue, respectively, and **n** the outward normal from the implant.

### 3.4. Equations for heat transfer and flow analysis in the tissue

Heat generated inside the implant (Section 3.3) is conducted into the surrounding tissue, where transport is governed by conduction and blood-flow–induced convection. The tissue is modeled as a homogeneous, isotropic porous medium saturated with blood/interstitial fluid. Material properties are treated as constant over the simulated range; phase change and chemical reactions are neglected.

The porous-media energy equation is

$$(\rho c)_{eff}\frac{\partial T}{\partial t} - \nabla\cdot\left(k_{eff}\nabla T\right) = -(\rho c)_b\mathbf{u}\cdot\nabla T + Q_{met} + Q_{e,t}, \tag{13}$$

with effective properties

$$(\rho c)_{eff} = \left(1-\varepsilon_p\right)(\rho c)_s + \varepsilon_p(\rho c)_b, \tag{14}$$

$$k_{eff} = \left(1-\varepsilon_p\right)k_s + \varepsilon_p k_b. \tag{15}$$

In this work, the effective thermal conductivity in Eq. (15) represents the stagnant (volume-averaged) conductivity of the porous tissue. Thermal dispersion and tortuosity-related corrections are not considered, as they typically require additional empirical parameters and are expected to have a secondary influence under low interstitial-flow conditions. Where $T$ is tissue temperature (K), **u** is the flow velocity (m/s), $\varepsilon_p$ is porosity (-), subscripts $s$ and $b$ denote solid matrix and blood/fluid phases, $Q_{met}$ is metabolic heat (W/m$^3$), and $Q_{e,t}$ is any external volumetric source in tissue (W/m$^3$). Heat released in the implant enters the tissue primarily via interfacial conduction through the continuity conditions in Eq. (12).

For comparison, the Pennes bioheat model [19] is written as.

$$(\rho c)_s\frac{\partial T_s}{\partial t} - \nabla\cdot(k_s\nabla T_s) = (\rho c)_b\omega_b(T_b - T_s) + Q_{met} + Q_{e,t}, \tag{16}$$

where $\omega_b$ is the blood perfusion rate (1/s) and $T_b$ is the arterial blood temperature (K). In this study, the arterial blood temperature $T_b$ was set to 37 °C to represent normal physiological conditions. Fluid motion in the porous tissue follows the Brinkman-extended Darcy equations with Boussinesq buoyancy [26]:

Continuity equation:

$$\nabla\cdot\mathbf{u} = 0 \tag{17}$$

Momentum equation:

$$\left(\frac{\rho}{\varepsilon_p}\right)\frac{\partial\mathbf{u}}{\partial t} + \left(\frac{\mu}{\kappa}\right)\mathbf{u} = -\nabla p + \nabla\cdot\left[\left(\frac{1}{\varepsilon_p}\right)\left(\mu\left(\nabla\mathbf{u} + (\nabla\mathbf{u})^T\right)\right)\right] + \rho\mathbf{g}\beta\left(T - T_{ref}\right) \tag{18}$$

where $\rho$ is the fluid density (kg/m$^3$), $\mu$ is the dynamic viscosity (N.s/m$^2$), $\kappa$ is the permeability of a porous tissue (m$^2$), $p$ is the pressure (N/m$^2$), **g** is the gravity (m/s$^2$), $\beta$ is the volume expansion coefficient (1/K), and $T_{ref}$ is the reference temperature considered here, which is 37 °C.

In the Brinkman porous-medium formulation, the permeability $\kappa$ governs viscous resistance to interstitial flow and thus plays an important role in heat convection within the tissue. To clarify its dependence on porosity, the present study assumes that permeability increases monotonically with porosity, owing to reduced flow resistance and enhanced pore connectivity. Following classical porous-media theory, this relationship can be approximated by a Kozeny–Carman-type correlation: [37]

$$\kappa\left(\varepsilon_p\right) = \frac{\varepsilon_p^3 d_p^2}{175(1-\varepsilon)^2}, \tag{19}$$

where $\kappa$ denotes permeability (m$^2$), ε is tissue porosity (-), and $d_p$ is the characteristic pore diameter (m). We set $d_p$=1 × 10$^{-4}$ m (100 μm) to isolate porosity effects. As indicated by Eq. (19), higher porosity corresponds to higher permeability, thereby facilitating fluid motion in the porous tissue and strengthening the convective contribution to heat transfer.

*Boundary and initial conditions.*

External tissue boundaries are maintained at normothermia, at 37 °C. Similarly, the arterial blood temperature $T_b$ in Eq. (16) was fixed at 37 °C as the reference temperature for perfusion heat exchange. Open (traction-free) flow boundaries allow fluid to enter/leave without artificial reflection,

$$\mathbf{n}\cdot\left[-p\mathbf{I}+\left(\frac{1}{\varepsilon_p}\right)\mu\left(\nabla\mathbf{u}+(\nabla\mathbf{u})^T\right)\right]=-f_0\cdot\mathbf{n} \tag{20}$$

with $\mathbf{n}$ the outward unit normal and $\mathbf{I}$ the identity tensor. The initial temperature is uniform,

$$T(t_0)=37^{\circ}C \tag{21}$$

In the present porous-media formulation, the velocity field is not prescribed through an imposed inlet blood velocity. Instead, the motion of the fluid phase arises naturally from buoyancy effects induced by temperature gradients generated during implant heating. This mechanism is represented through the Boussinesq approximation term in the Brinkman momentum equation, which introduces a body force proportional to the temperature difference relative to the reference temperature. This modeling approach represents interstitial fluid motion within the porous tissue rather than macroscopic blood flow in large vessels. As discussed in the literature, prescribing realistic blood velocities and directions in biological tissues is challenging due to the complex and heterogeneous structure of vascular networks. Several studies therefore adopt porous-media formulations to represent the averaged transport effects of perfusion and interstitial flow without explicitly resolving individual vessels [34–36]. Consequently, fluid motion in the present model develops self-consistently from the coupled thermal–fluid equations, while the boundary condition in Eq. (18) allows fluid to enter or leave the computational domain without imposing a prescribed flow direction.

Boundary and initial conditions (summary):

- Electromagnetics (induction): a 2D axisymmetric domain with the symmetry axis at $r = 0$; open-space truncation using infinite-element domains with a magnetic-insulation boundary at the outer boundary to suppress reflections.
- Heat transfer: external tissue boundaries maintained at normothermia (37 °C); thermal continuity at the implant–tissue interface (continuous temperature and normal heat flux); uniform initial temperature $T(t_0)$=37 °C.
- Porous flow (Brinkman–Darcy): open (traction-free) boundaries allowing inflow/outflow without prescribing a flow direction; buoyancy-driven flow represented via the Boussinesq body-force term with $T_{ref}$=37 °C.

### 3.5. Calculation procedure

The finite element method (FEM) was employed to solve the coupled electromagnetic–thermal–fluid equations together with the prescribed initial and boundary conditions on a 2D axisymmetric domain. The EM problem was solved in the frequency domain to obtain volumetric power sources for the transient thermal and porous-flow analyses; material properties were taken as constant, yielding a one-way coupling from electromagnetic to thermal/flow. An adaptive mesh refinement strategy was applied with local densification near the implant–tissue interface and other high-gradient regions; a grid of $\sim 1 \times 10^4$ elements was found adequate by mesh-convergence checks. All simulations were carried out in COMSOL™ Multiphysics, which provided a unified environment for electromagnetic field computation, heat generation and conduction, and Brinkman porous-media flow. This computational procedure ensures consistency between the EM power deposition and the resulting thermal–fluid response in tissue.

## 4. Results and discussion

This section examines the effects of tissue porosity, magnetic flux density, and implant geometry on heat-transfer behavior. The numerical framework follows the experimental setup in Section 2 for direct comparison with phantom measurements. Results are presented in four parts: model validation, electromagnetic-field characterization, parametric analyses, and clinical-implication discussion. The present 2D axisymmetric model is valid for the coaxial coil–implant configuration considered here; however, it does not capture off-axis misalignment, asymmetric field perturbations, or tissue heterogeneity, which would require a full 3D formulation and may affect local peak temperatures.

### 4.1. Model validation

Validation was performed under the same conditions as the liver-phantom experiment. The implant was exposed to a 190 kHz alternating magnetic field with a magnetic flux density of approximately 6.0 mT. The induction coil supplied 845 W of input power. Temperature was measured 1 mm from the implant surface using a fiber-optic sensor, and the corresponding computational point was used for comparison. For validation, the electromagnetic excitation parameters in the numerical model were matched to those of the experiment.

For the validation experiment (Fig. 3), the liver phantom was not wrapped with additional thermal insulation. This was intentional, because a perfectly insulated exterior would unrealistically confine heat and overpredict the temperature rise. Instead, the phantom was allowed to exchange heat with the surrounding environment, which better represents practical conditions.

It is also worth noting that the electromagnetic induction field is primarily localized around the coil–implant region, so heating is generated locally within the conductive/ferromagnetic implant (eddy-current/Joule heating with magnetic-loss contribution), rather than by volumetric EM deposition throughout the phantom. However, thermal confinement is a separate issue from EM localization; therefore, we explicitly account for heat dissipation at the phantom exterior.

Accordingly, the numerical model applies a constant-temperature boundary at the outer phantom/tissue boundary (37 °C) to represent controlled thermal coupling to the surroundings and to avoid artificial heat accumulation.

Fig. 4 presents a comparison of temperature evolution at the monitoring point near the implant surface, as predicted by both the Pennes bioheat and porous-media models, alongside experimental measurements. The porous-media model demonstrates strong concordance with experimental data, especially during the transient heating phase (0–60 s). Conversely, the Pennes bioheat equation overestimates the maximum temperature rise due to its treatment of perfusion as a spatially uniform heat sink.

The improved predictive accuracy of the porous-media model is attributed to its explicit incorporation of interstitial flow and convective transport, which more accurately redistributes heat within the tissue microstructure. These results are consistent with the findings of Khaled and Vafai [21] and Mahjoob and Vafai [23], who showed that flow-induced convection enhances the effective thermal conductivity of porous biological tissues.

Overall, this validation confirms that the coupled electromagnetic–porous media framework can accurately predict transient temperature responses in implant-embedded tissue. The validated model is therefore employed in the subsequent simulations (Sections 4.2–4.5) to examine the influence of electromagnetic field strength, tissue porosity, and implant diameter, including the emergence of the critical implant size identified in this study.

### 4.2. Electromagnetic field distribution

Fig. 5 illustrates the magnetic-field intensity distribution obtained

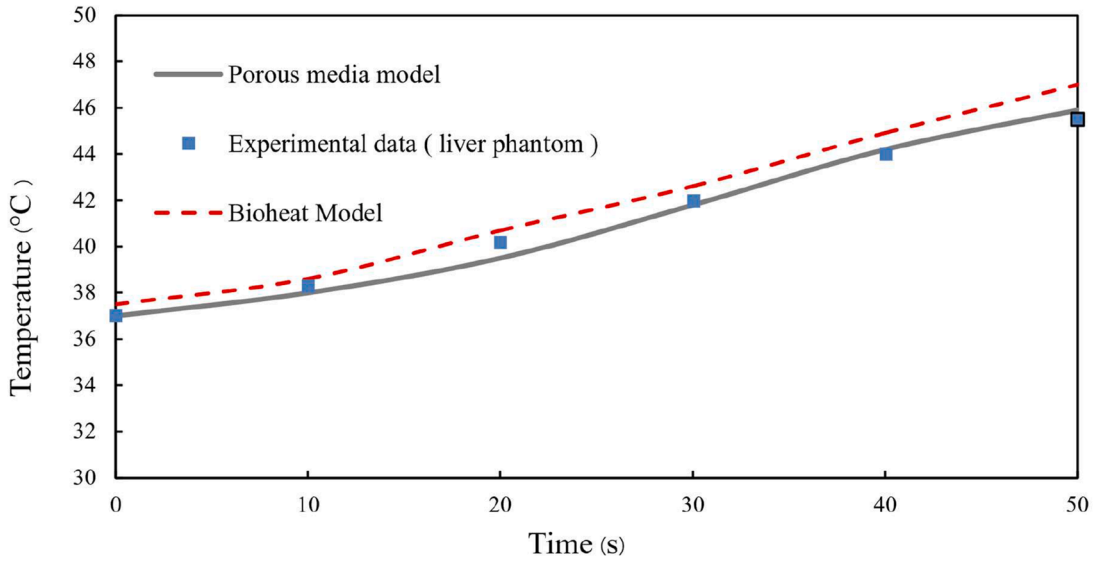


**Fig. 4.** Comparison of temperature evolution from the porous-media and bioheat models with experimental data in the liver phantom.

from the electromagnetic simulation performed under the same excitation conditions used in the thermal analysis—namely, an input power of 100 W delivered to a three-turn circular induction coil (10 mm diameter) operating at 100 kHz. As shown in Fig. 5(a), the magnetic field is strongly confined to the near-field region surrounding the coil, exhibiting rapid radial attenuation as expected for high-frequency induction systems. Fig. 5(b) provides an enlarged view of the region near the implant, where the magnetic-field intensity reaches its maximum along the implant surface. This localized field concentration leads to strong eddy-current induction within the ferromagnetic rod and represents the primary source of resistive heating that initiates subsequent thermal conduction and convection in the surrounding tissue.

Consequently, the eddy-current density and Joule-heating rate reach their maximum within the metallic implant, resulting in localized heat generation that initiates conduction and convective transfer into the surrounding tissue. These observations align with previous induction-heating analyses [12], [13], which confirm that energy deposition is primarily restricted to the near-field region of the excitation coil, thereby determining heating efficiency in ferromagnetic implant hyperthermia (FIH).

The analysis highlights that the magnetic field is strongly localized around the implant–tissue interface, with intensity rapidly decaying away from the coil axis. This spatial confinement governs the region of effective Joule heating and defines the boundary of energy deposition during ferromagnetic implant hyperthermia.

### 4.3. Effect of tissue porosity

Simulations were performed under identical electromagnetic excitation (magnetic flux density $B$ = 11.5 mT, frequency = 100 kHz, heating duration = 30 s). Fig. 6 shows how tissue porosity affects local temperature and flow fields. As porosity increases ($\varepsilon = 0.2$, 0.4, and 0.6), the maximum interstitial-fluid velocity rises from $1.74 \times 10^{-4}$ m/s to $2.79 \times 10^{-4}$ m/s, enhancing convective mixing and spreading the thermal plume. As a result, the maximum temperature decreases slightly from 46.7 °C to 46.5 °C; although the change is small, the trend is systematic and reflects enhanced convective heat removal around the implant, as evidenced by increasingly diffuse isothermal contours.

This trend is due to increased effective permeability ($\kappa$) and reduced viscous resistance in porous tissue, which promote stronger interstitial circulation and facilitate convective heat removal from the implant–tissue interface. These results confirm that higher porosity enhances convective cooling and heat dispersion, while low-porosity tissues confine heat more effectively, creating localized hot spots favorable for ablation.

Fig. 7 further quantifies the relationship between porosity and maximum tissue temperature at various heating durations (10, 20, and 30 s). The weak dependence of $T_{max}$ on $\varepsilon$ under short exposure times indicates that convection becomes dominant only after sufficient heating duration, when buoyancy-driven flow is fully developed. At higher porosity, the increased permeability ($\kappa$) promotes fluid circulation that redistributes thermal energy away from the implant surface, resulting in lower steady-state temperatures. This finding agrees with the theoretical prediction of Brinkman–Darcy flow, where the convective term becomes more significant as the pore-scale Peclet number increases. Similar convective enhancement was reported by Wessapan and Rattanadecho [24] in ultrasound-induced heating of porous tissue. Importantly, while porosity modulates the spatial characteristics of heating, it does not alter the fundamental nonlinear relationship between implant size and maximum temperature observed in Section 4.5. The porosity values used in this study ($\varepsilon = 0.2$–$0.6$) represent an effective parameter describing the fraction of interstitial fluid and vascular space within porous biological tissue. In many biological heat-transfer studies, effective porosity values around $\varepsilon \approx 0.2$ are commonly adopted to represent typical soft tissues. However, higher values may be considered in parametric analyses to account for increased vascularization, enhanced permeability, or pathological conditions in which the effective pore space is enlarged.

The purpose of considering this wider porosity range is to evaluate the sensitivity of implant-induced heating to variations in porous transport properties. As shown in Figs. 6–7, increasing porosity enhances interstitial convection and slightly reduces the maximum temperature due to stronger heat dispersion. Nevertheless, the overall temperature variation remains relatively small, indicating that the dominant mechanism governing the heating process is the electromagnetic power deposition in the implant rather than the precise value of tissue porosity. The emergence of a critical implant size is governed primarily by the balance between electromagnetic power deposition and thermal dissipation, rather than by tissue porosity.

### 4.4. Effect of magnetic flux density

The simulations were performed using the porous-media model under identical geometric and thermal boundary conditions, with a fixed implant diameter of 1 mm, heating duration of 60 s, and tissue porosity of 0.4. The magnetic flux density $B$ was varied at 8.16, 11.5, and 14.1 mT to investigate its influence on the temperature evolution. The

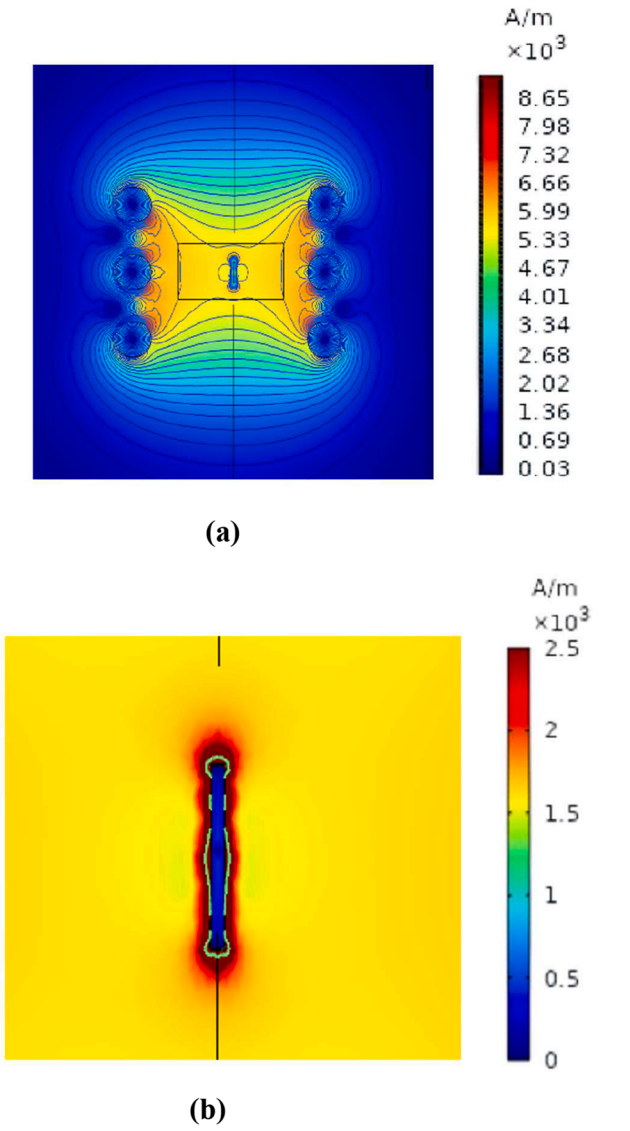


**Fig. 5.** Magnetic field intensity (A/m) in the tissue phantom: (a) overall distribution around the coil and (b) detailed field near the implant.

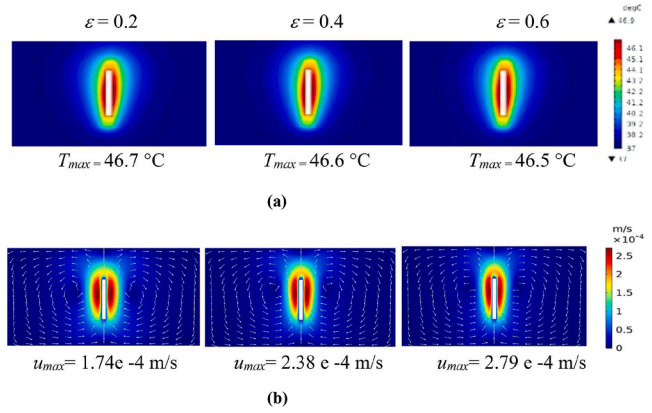


**Fig. 6.** Temperature (a) and velocity (b) distributions around the implant under different tissue porosities ($\varepsilon$ = 0.2, 0.4 and 0.6) based on porous-media model.

magnetic field in this study is an alternating (time-varying) near-field generated by an induction coil driven by AC. Unlike MRI, which uses strong static fields on the order of 1–2 T for imaging, the present induction-heating configuration operates in the millitesla range, where time-varying fields induce eddy currents in the conductive implant and produce Joule heating. The magnetic flux density values in Fig. 8 are obtained from electromagnetic simulations of the coil under the operating frequency and input power used in the validation setup, yielding local values of approximately 8–14 mT near the implant region. Fig. 8 presents the time-dependent maximum tissue temperature for these magnetic-field intensities.

The temperature rise shows a nearly quadratic dependence on magnetic flux density, consistent with stronger eddy current induction at higher $B$. Increasing $B$ intensifies eddy-current induction within the ferromagnetic implant, resulting in higher power dissipation and faster heating rates. The strongest coupling occurs near the implant surface, where induced current density is highest.

At the highest field strength (14.1 mT), the peak tissue temperature rises to approximately 51 °C after 60 s, indicating that stronger magnetic excitation substantially enhances Joule heating within the implant. Although Fig. 8 reports only the peak temperature, the porous-media model predicts that higher $B$ also enhances buoyancy-driven interstitial motion, which contributes to moderating local thermal gradients. This trend is consistent with the reduced curvature of the temperature-time curve at late heating times, reflecting the increasing influence of convective heat dispersion at elevated temperatures.

### 4.5. *Effect of implant diameter*

To investigate the geometric influence on heat generation, a parametric study was conducted using the porous-media model with fixed electromagnetic excitation ($B$ = 11.5 mT, frequency = 100 kHz, heating duration = 60 s). In this study, the implant was modeled as a cylindrical rod with fixed length while the diameter was varied to investigate the geometric influence on electromagnetic heating. The diameter directly affects the induced current distribution within the implant as well as the thermal contact area between the implant and the surrounding tissue. Therefore, it represents a key geometric parameter governing both power absorption and heat dissipation. Alternative geometric modifications, such as varying implant orientation or modifying the implant shape while maintaining constant volume, may also influence the heating behavior by altering the electromagnetic coupling and the effective contact area with tissue. However, the present analysis focuses on isolating the role of implant diameter in order to identify the existence of a critical size governing the heating response. Investigation of more complex implant geometries and orientations would require full three-dimensional modeling and will be addressed in future studies. The implant diameter was systematically varied between 0.2 mm and 8 mm while keeping all other physical and boundary conditions constant.

Fig. 9 shows the relationship between implant size and maximum tissue temperature at three heating durations (10, 30, and 60 s). The results reveal a non-monotonic dependence of temperature on implant size. The peak temperature increases as the implant diameter grows from 0.2 to approximately 1 mm, reflecting enhanced magnetic coupling and greater eddy-current generation within the metallic volume. Beyond this critical diameter (~1 mm), the maximum temperature progressively decreases as conductive and convective heat losses become more effective at removing heat from the implant–tissue interface.

This nonlinear response results from the skin-depth limitation of electromagnetic induction, where only a finite region near the implant surface significantly contributes to heat generation. Therefore, excessively large implants do not improve heating efficiency but may expand the affected thermal region. These findings suggest that an optimal implant diameter can achieve effective therapeutic heating while minimizing collateral thermal spread.

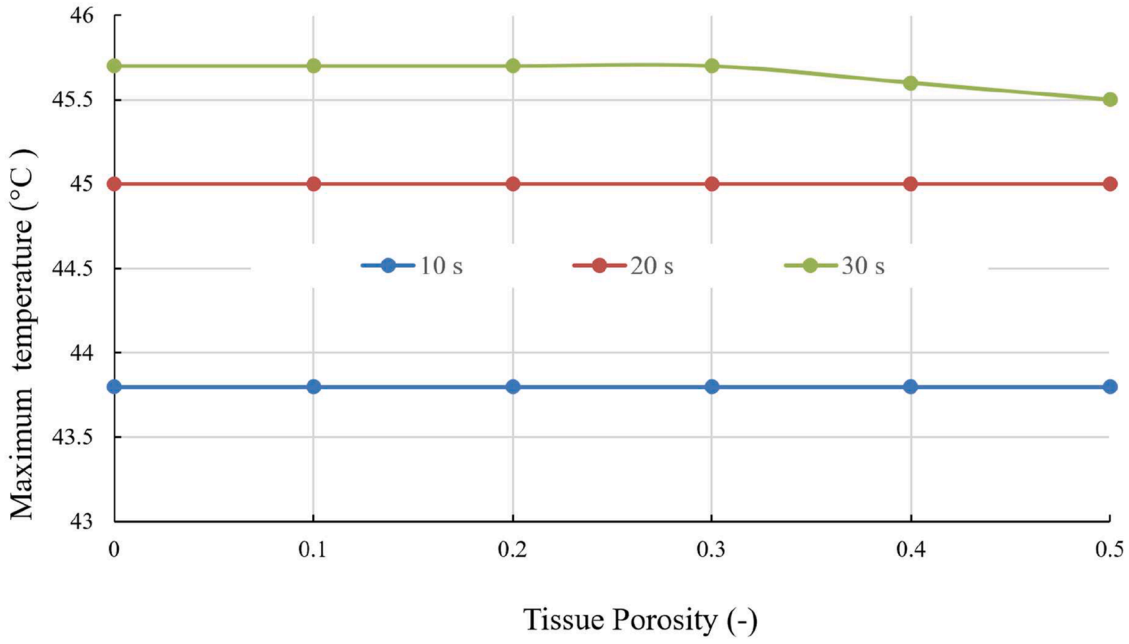


**Fig. 7.** Maximum tissue temperature at different tissue porosities ($\varepsilon$ = 0–0.5) for various heating times (10 s, 20 s, and 30 s).

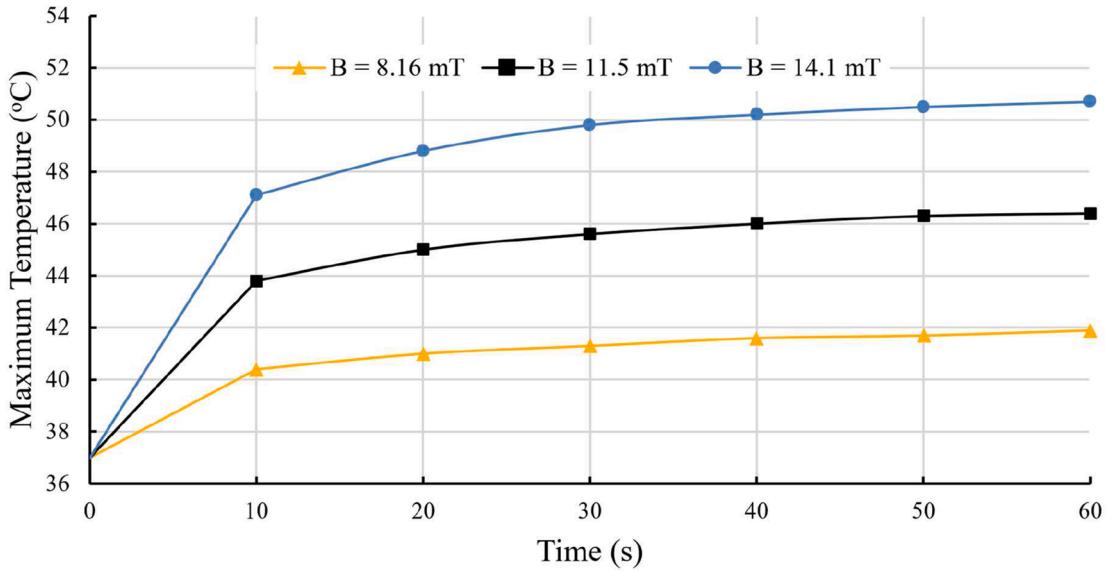


**Fig. 8.** Temporal evolution of maximum tissue temperature at the implant surface under different magnetic flux densities ($B$ = 8.16 mT, 11.5 mT, and 14.1 mT).

### *4.6. Physical interpretation and implications for treatment planning*

The combined results of this study clarify the fundamental heat-transfer mechanisms governing ferromagnetic implant hyperthermia in porous tissue. The porous-media formulation demonstrates that interstitial convection, driven by tissue porosity and permeability, plays a critical role in redistributing heat away from the implant surface. This convective transport moderates excessive temperature gradients and enhances thermal uniformity compared to predictions from the conventional Pennes bioheat model. These findings underscore the importance of considering microvascular flow effects when modeling localized electromagnetic heating.

A key physical insight from this study is the emergence of a critical implant size beyond which additional increases in diameter no longer enhance heating efficiency. While larger implants strengthen eddy-current induction and initially increase temperature, thermal dissipation through conduction and buoyancy-driven interstitial flow eventually dominates, producing a non-monotonic relationship between implant size and peak temperature. This nonlinear behavior arises from the combined effects of electromagnetic skin-depth limitations and tissue-dependent thermal losses, revealing a size-governed thermal regime that has not been previously characterized in ferromagnetic implant hyperthermia.

From a treatment-planning and device-design perspective, these findings highlight the importance of accounting for both tissue microstructure and implant geometry when planning hyperthermia treatments. Models that neglect convective effects or assume monotonic heating with implant size may significantly misestimate therapeutic temperatures, particularly in highly vascularized organs.

Although explicit tissue-damage modeling is beyond the scope of the present work, the predicted temperature–time histories can be interpreted in the context of standard hyperthermia thresholds commonly

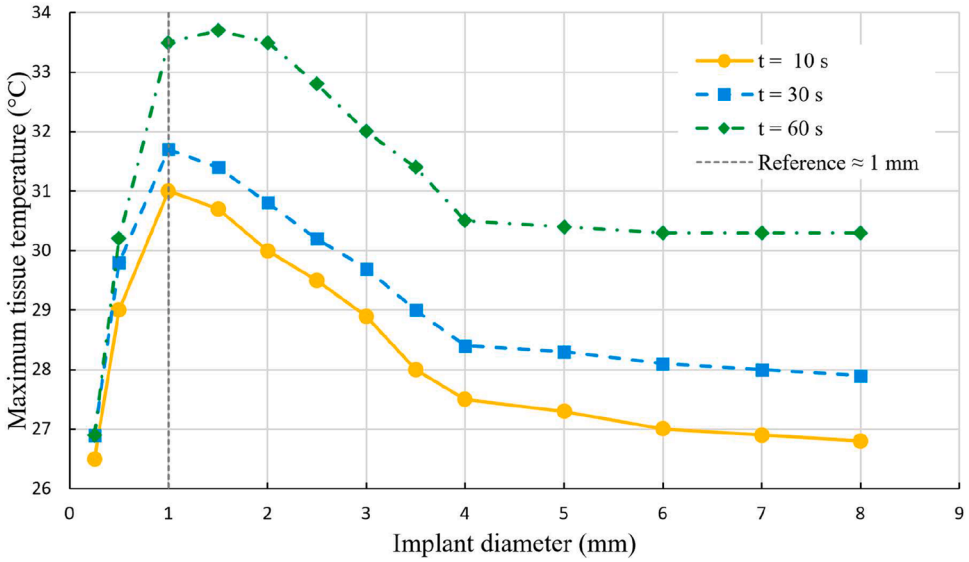


**Fig. 9.** Maximum tissue temperature versus implant diameter for $t = 10$ s, 30 s, and 60 s.

used in hyperthermia and ablation. Thermal damage metrics (e.g., CEM43 or Arrhenius-type integrals) can be computed directly from the predicted temperature–time histories, evaluated at representative tissue locations such as the hottest region near the implant–tissue interface. A quantitative thermal-dose assessment is beyond the present scope and is identified as an important extension for future work. Future extensions of the framework will incorporate Arrhenius-type damage models to translate the identified critical implant size and field-strength regimes into quantitative estimates of necrotic-zone extent. Despite strong agreement between simulations and phantom experiments, certain simplifying assumptions remain. The present axisymmetric model uses constant material properties and steady perfusion, and does not incorporate temperature-dependent viscosity, damage kinetics, or perfusion feedback. Future work should incorporate these physiological effects and extend the framework to full 3D anatomical domains with real-time thermometry integration to support relevant treatment-planning scenarios.

The proposed ferromagnetic implant hyperthermia approach can be compared with commonly used thermal ablation techniques such as radiofrequency ablation (RFA) and microwave ablation (MWA). In RFA, heat is generated via resistive heating from currents flowing in tissue, whereas MWA produces heating via dielectric losses under microwave fields. In contrast, the present approach relies on induction heating of a ferromagnetic implant placed within the target tissue, where an alternating magnetic field induces eddy currents (with a magnetic-loss contribution) that generate heat which then propagates into surrounding tissue through conduction and convection.

From a heat-transfer perspective, implant-mediated heating may provide localized energy deposition and a heating pattern that can be tuned through implant geometry and excitation conditions. However, it also introduces practical considerations, particularly implantation logistics and device clearance/removal, compared with RFA/MWA probes that can be removed after treatment. Despite these limitations, the present results suggest that implant-mediated induction heating can produce predictable thermal responses governed by the balance between electromagnetic power deposition and tissue heat dissipation and may therefore serve as a complementary strategy when localized and controllable heating is desired.

## 5. Conclusion

This study developed and experimentally validated a fully coupled electromagnetic–thermal modeling framework to analyze heat generation and dissipation in ferromagnetic implants embedded within porous biological tissue. By integrating Maxwell-based eddy-current modeling with both Pennes and porous-media heat-transfer formulations, the model accurately captured transient temperature evolution in liver-phantom experiments. The porous-media model, in particular, demonstrated superior predictive capability due to its explicit representation of interstitial convection.

A central finding of this study is the nonlinear dependence of heating efficiency on implant diameter. While larger implants enhance magnetic coupling and accelerate eddy-current heating, conduction- and convection-driven thermal losses eventually dominate, leading to a critical implant size beyond which additional diameter no longer increases the maximum temperature. Tissue porosity further modulates these dynamics by enhancing interstitial convection and smoothing local temperature gradients; however, the emergence of the critical-size threshold is governed primarily by the balance between electromagnetic power deposition and tissue thermal dissipation. This previously uncharacterized mechanism provides a new physical basis for optimizing implant geometry and magnetic-field parameters in ferromagnetic implant hyperthermia.

Overall, the validated framework establishes a physically robust basis for optimizing implant geometry, magnetic-field strength, and treatment parameters. Future work should extend this approach to three-dimensional, patient-specific anatomical models and incorporate temperature-dependent perfusion and tissue-damage kinetics to further improve the translational applicability of the proposed framework to realistic hyperthermia treatment planning. The identification of a critical implant size provides an important guideline for safe and effective design of implant-assisted hyperthermia protocols.

**Declaration of AI and AI-assisted technologies in the writing processDuring the preparation of this manuscript, the authors used ChatGPT (OpenAI) to assist in improving the clarity, organization, and grammar of the text. After using this tool, the authors reviewed and edited the content as needed and take full responsibility for the content of this publication.**

*Nomenclature*

| | |
|---|---|
| $A$ | magnetic vector potential (Wb/m) |
| $B$ | magnetic flux density (T) |
| $c$ | specific heat capacity (J/(kg·K)) |

| | |
|---|---|
| $D$ | electric displacement or electric flux density (C/m$^2$) |
| $E$ | electric field intensity (V/m) |
| $e$ | electric vector field (-) |
| $f$ | normal stress (N/m$^2$) |
| $g$ | gravitational acceleration (m/s$^2$) |
| $H$ | magnetic field intensity (A/m) |
| $h$ | convection coefficient (W/m$^2$·K) |
| $J$ | electric current density (A/m$^2$) |
| $i$ | imaginary unit (-) |
| $k$ | thermal conductivity (W/(m·K)) |
| $k_{\text{eff}}$ | effective thermal conductivity (W/m·K) |
| $N$ | number of turns in the induction coil (-) |
| $n$ | unit normal vector (-) |
| $p$ | pressure (Pa) |
| $(\rho c)_{\text{eff}}$ | effective volumetric heat capacity (J/ (m$^3$·K)) |
| $Q$ | volumetric heat source (W/m$^3$) |
| $Q_e$ | electromagnetic heat source (W/ m$^3$) |
| $Q_{rh}$ | resistive (ohmic) loss (W/ m$^3$) |
| $Q_{ml}$ | magnetic loss (W/ m$^3$) |
| $Q_{met}$ | metabolic heat generation (W/ m$^3$) |
| $T$ | temperature ( °C) |
| $T_b$ | blood/ arterial temperature ( °C) |
| $T_i$ | implant temperature ( °C) |
| $T_t$ | tissue temperature ( °C) |
| $t$ | time (s) |
| $u$ | velocity vector (m/s) |
| $V$ | electric potential (V) |

*Greek letters*

| | |
|---|---|
| $\mu$ | magnetic permeability (H/m) |
| $\mu_r$ | relative magnetic permeability (-) |
| $\varepsilon$ | permittivity (F/m) |
| $\varepsilon_r$ | relative permittivity (-) |
| $\varepsilon_p$ | porosity (-) |
| $\kappa$ | permeability of porous tissue (m$^2$) |
| $\sigma$ | electric conductivity (S/m) |
| $\rho$ | density (kg/m$^3$) |
| $\omega$ | angular frequency (rad/s) |
| β | thermal expansion coefficient (1/K) |
| $\omega_b$ | blood perfusion rate (1/s) |

*Subscripts*

| | |
|---|---|
| $b$ | blood |
| $e$ | external |
| $i$ | implant |
| $t$ | tissue |
| $s$ | solid matrix |
| $met$ | metabolic |
| $ml$ | magnetic loss |
| $r$ | relative |
| $0$ | free space or initial condition |

## CRediT authorship contribution statement

**Pongsavat Savatdipap:** Writing – original draft, Visualization, Validation, Investigation, Formal analysis. **Teerapot Wessapan:** Writing – review & editing, Project administration, Methodology, Investigation, Funding acquisition, Conceptualization. **Manop Yamfang:** Supervision, Resources. **Phadungsak Rattanadecho:** Supervision, Funding acquisition.

## Declaration of competing interest

The authors declare that they have no known competing financial interests or personal relationships that could have appeared to influence the work reported in this paper.

## Acknowledgments

This study was supported by the National Science, Research, and Innovation Fund, Thailand Science Research and Innovation (TSRI) through Rajamangala University of Technology Thanyaburi (FRB68E0704) (Grant No. FRB680045/0168). The authors gratefully acknowledge the Thailand Science Research and Innovation Fundamental Fund for the fiscal year 2025 and 2026.

## Data availability

The authors do not have permission to share data.

## References

[1] J.W. Strohbehn, E.B. Douple, Hyperthermia and Cancer Therapy: A review of biomedical engineering contributions and challenges, IEEE Trans. Biomed. Eng. 31 (1984) 779–787.
[2] S.P. Tomasovic, Biological basis for hyperthermia in cancer treatment, in: Proc. Annu. Int. Conf, IEEE Eng. Med. Biol. Soc, 1988, pp. 860–861.
[3] S. Bae, S.W. Lee, A. Hirukawa, Y. Takemura, Y.H. Jo, S.G. Lee, AC magnetic-field-induced heating and physical properties of ferrite nanoparticles for a hyperthermia agent in medicine, IEEE Trans. Nanotechnol. 8 (2009) 86–94.
[4] R. Zuchini, H.W. Tsai, C.Y. Chen, C.H. Huang, S.C. Huang, G.B. Lee, C.F. Huang, X. Z. Lin, Electromagnetic thermotherapy using fine needles for hepatoma treatment, Eur. J. Surg. Oncol. 37 (2011) 604–610.
[5] C.C. Chen, C.C. Tai, S.J. Huang, Y.H. Chen, C.H. Lin, Thermotherapy induction heating apparatus with new magnetic-wrapped coil design, IEEE Trans. Ind. Electron. 61 (2014) 2592–2600.
[6] A. Jordan, P. Wust, H. Fahling, W. John, A. Hinz, R. Felix, Inductive heating of ferromagnetic particles and magnetic fluid: physical evaluation of their potential for hyperthermia, Int. J. Hypertherm. 9 (1993) 51–68.
[7] A. Jordan, R. Scholz, P. Wust, H. Fähling, R. Felix, Magnetic fluid hyperthermia (MFH): cancer treatment with AC magnetic field induced excitation of biocompatible superparamagnetic nanoparticles, J. Magn. Magn. Mater. 201 (1999) 413–419.
[8] A. Jordan, R. Scholz, K. Maier-Hauff, M. Johannsen, P. Wust, J. Nadobny, H. Schmidt, S. Deder, S. Loening, W. Lanksch, R. Felix, Presentation of a new magnetic field therapy system for the treatment of human solid tumors with magnetic fluid hyperthermia, J. Magn. Magn. Mater. 225 (2001) 118–126.
[9] S.C. Huang, J.W. Kang, H.W. Tsai, Y.S. Shan, X.Z. Lin, G.B. Lee, Electromagnetic thermotherapy system with needle arrays: A practical tool for the removal of cancerous tumors, IEEE Trans. Biomed. Eng. 61 (2014) 598–605.
[10] Y.J. Chao, Y.S. Shan, R. Zuchini, H.W. Tsai, P.W. Lin, G.B. Lee, X.Z. Lin, Successfully seal pancreatic end after thermal distal pancreatectomy using needle arrays in alternating electromagnetic fields, Surg. Innov. 20 (2013) 150–157.
[11] S.C. Huang, Y.Y. Chang, Y.J. Chao, Y.S. Shan, X.Z. Lin, G.B. Lee, Dual-row needle arrays under an electromagnetic thermotherapy system for bloodless liver resection surgery, IEEE Trans. Biomed. Eng. 59 (2012) 824–831.
[12] I. Lope, J. Acero, C. Carretero, Analysis and optimization of the efficiency of induction heating applications with litz-wire planar and solenoidal coils, IEEE Trans. Power Electron. 31 (2016) 5089–5101.
[13] C. Li, Y. Zhou, P. Wang, X. Wang, S. Dong, J. Du, Z. Liao, C. Yao, J. Tan, Y. Mi, Design and experiments of electromagnetic heating forming technology, IEEE Access 7 (2019) 62646–62656.
[14] W. Han, K.T. Chau, Z. Zhang, C. Jiang, Single-source multiple-coil homogeneous induction heating, IEEE Trans. Magn. 53 (2017) 1–6.
[15] J.R. Oleson, A review of magnetic induction methods for hyperthermia treatment of cancer, IEEE Trans. Biomed. Eng. 31 (1984) 91–97.
[16] C.C. Tai, C.C. Chen, C.C. Kuo, F.W. Lin, C.J. Chang, Y.H. Chen, W.C. Wang, Deep-magnetic-field generator using flexible laminated copper for thermotherapy applications, IEEE Trans. Magn. 50 (2014) 1–4.
[17] C.J. Chang, C.C. Tai, F.W. Lin, C.C. Kuo, C.M. Hung, Effects of flexible induction coil pitch on the heating performance of thermotherapy needles, IEEE Trans. Instrum. Meas. 69 (2020) 8983–8991, https://doi.org/10.1109/TIM.2020.2998302.
[18] T. Wessapan, P. Rattanadecho, N. Somsuk, M. Yamfang, M. Guptasa, P. Montienthong, Thermal effects of electromagnetic energy on skin in contact with metal: a numerical analysis, Energies 16 (2023) 5925, https://doi.org/10.3390/en16165925.
[19] H.H. Pennes, Analysis of tissue and arterial blood temperatures in the resting human forearm, J. Appl. Physiol. 1 (1948) 93–122.
[20] C.H. Wang, Z.Y. Liu, Z.Y. Jiang, X.X. Zhang, Numerical investigations of convection heat transfer in a thermal source-embedded porous medium via a lattice Boltzmann method, Case Stud. Therm. Eng. 29 (2022) 101758, https://doi.org/10.1016/j.csite.2022.101758.
[21] A.R. Khaled, K. Vafai, The role of porous media in modeling flow and heat transfer in biological tissues, Int. J. Heat Mass Transf. 46 (2003) 4989–5003, https://doi.org/10.1016/S0017-9310(03)00301-6.
[22] K. Khanafer, K. Vafai, The role of porous media in biomedical engineering as related to magnetic resonance imaging and drug delivery, Heat Mass Transf. 42 (2006) 939–953, https://doi.org/10.1007/s00231-006-0142-6.

[23] S. Mahjoob, K. Vafai, Analytical characterization of heat transport through biological media incorporating hyperthermia treatment, Int. J. Heat Mass Transf. 52 (2009) 1608–1618, https://doi.org/10.1016/j.ijheatmasstransfer.2008.07.038.
[24] T. Wessapan, P. Keangin, P. Rattanadecho, N. Somsuk, Comparative analysis of heat transfer dynamics in high-intensity focused ultrasound and microwave ablation for cancer treatment, Int. J. Thermofluids 26 (2025) 101090, https://doi.org/10.1016/j.ijft.2025.101090.
[25] S. Hossain, S.M. Chapal Hossain, M. Ferdows, M. Zavid Iqbal Bangalee, M. Shariful Alam, Computer simulation based analysis of transient two-phase thermal evolutions during multiprobe cryosurgery of hepatic tissues embedded without or with blood vessels, Int. J. Thermofluids 21 (2024) 100587, https://doi.org/10.1016/j.ijft.2024.100587.
[26] H.C. Brinkman, A calculation of the viscous force exerted by a flowing fluid on a dense swarm of particles, Appl. Sci. Res. A1 (1949) 27–34, https://doi.org/10.1007/BF02120313.
[27] H.E. Boyer, in: T.L. Gall (Ed.), Metals Handbook, American Society for Metals, Materials Park, OH, 1985.
[28] S. Kaur, P.S. Mann, Comparison of single slot and double slot antenna for the treatment of hepatocellular carcinoma, Int. J. Res. Comput. Appl. Robot. 2 (5) (2014) 86–91.
[29] E.H. Ooi, V. Popov, M. Alfano, J.K.K. Cheong, Influence of natural convection on gold nanorods-assisted photothermal treatment of bladder cancer in mice, Int. J. Hypertherm. 37 (1) (2020) 634–650, https://doi.org/10.1080/02656736.2020.1771437.
[30] P. Gupta, A. Srivastava, Non-Fourier transient thermal analysis of biological tissue phantoms subjected to high intensity focused ultrasound, Int. J. Heat Mass Transf. 136 (2019) 1052–1063, https://doi.org/10.1016/j.ijheatmasstransfer.2019.03.014.
[31] X. Luo, H. Xie, Y. Ma, D. Lan, G. Wu, Z. Jia, Advances in Fe-based electromagnetic wave absorbers: multiscale engineering from atomic defects to macroscopic architectures for performance optimization, Int. J. Miner. Metall. Mater. 33 (3) (2026) 768–797, https://doi.org/10.1007/s12613-025-3252-1.
[32] X. Du, F. Yan, M. Cheng, H. Li, C. Peng, Y. Liu, D. Liu, D. Lan, G. Wu, Z. Jia, Dual-functional core-shell composites: integrated microwave absorption and thermal management properties, Int. J. Miner. Metall. Mater (2025).
[33] A. Andreozzi, M. Iasiello, C. Tucci, An overview of mathematical models and modulated-heating protocols for thermal ablation, Adv. Heat Transf. 52 (2020) 489–541, https://doi.org/10.1016/bs.aiht.2020.07.003.
[34] A. Cafarchio, M. Iasiello, G.P. Vanoli, A. Andreozzi, Microwave ablation modeling with AMICA antenna: validation by means a numerical analysis, Comput. Biol. Med. 167 (2023) 107669, https://doi.org/10.1016/j.compbiomed.2023.107669.
[35] M. Chaichanyut, S. Tungjitkusolmun, Microwave ablation using four-tine antenna: effects of blood flow velocity, vessel location, and total displacement on porous hepatic cancer tissue, Comput. Math. Methods Med. 2016 (2016) 4846738, https://doi.org/10.1155/2016/4846738.
[36] A. Andreozzi, L. Brunese, M. Iasiello, C. Tucci, G.P. Vanoli, Numerical investigation of a thermal ablation porous media-based model for tumoral tissue with variable porosity, Computation 9 (5) (2021) 50, https://doi.org/10.3390/computation9050050.
[37] P. Rattanadecho, P. Keangin, Numerical study of heat transfer and blood flow in two-layered porous liver tissue during microwave ablation process using single and double slot antenna, Int. J. Heat Mass Transf. 58 (1–2) (2013) 457–470.